PCCP

Electron transfer rate modulation with mid-IR in butadiyne-bridged donor-bridge-acceptor compounds

Journal:	*Physical Chemistry Chemical Physics*
Manuscript ID	CP-ART-07-2023-003175.R2
Article Type:	Paper
Date Submitted by the Author:	21-Nov-2023
Complete List of Authors:	Mendis, Kasun; Tulane University, Department of Chemistry Li, Xiao; Tulane University Valdiviezo Mora, Jesús del Carmen; Duke University, Chemistry Cox, Susannah; Purdue University, Department of Chemistry Zhang, Peng; Duke University, Chemistry Ren, Tong; Purdue University Beratan, David; Duke University, Department of Chemistry Rubtsov, Igor; Tulane University, Department of Chemistry

Electron transfer rate modulation with mid-IR in butadiyne-bridged donor-bridge-acceptor compounds

Kasun C. Mendis,[a] Xiao Li,[a] Jesús Valdiviezo,[b] Susannah D. Banziger,[e] Peng Zhang,[b] Tong Ren,[e] David N. Beratan,[b,c,d] and Igor V. Rubtsov[a*]

[a] *Department of Chemistry*, *Tulane University, New Orleans, LA 70118, USA*
[b] *Department of Chemistry*, *Duke University, Durham, North Carolina 27708, USA*
[c] *Department of Physics*, *Duke University, Durham, North Carolina 27708, USA*
[d] *Department of Biochemistry*, *Duke University, Durham, North Carolina 27710, USA*
[e] *Department of Chemistry*, *Purdue University, West Lafayette, Indiana 47907, USA*

Abstract

Controlling electron transfer (ET) processes in donor-bridge-acceptor (DBA) compounds by mid-IR excitation can enhance our understanding of the ET dynamics and may find practical applications in molecular sensing and molecular-scale electronics. Alkyne moieties are attractive to serve as ET bridges, as they offer the possibility of fast ET and present convenient vibrational modes to perturb the ET dynamics. Yet, these bridges introduce complexity because of the strong torsion angle dependence of the ET rates and transition dipoles among electronic states and a shallow torsion barrier. In this study, we implemented ultrafast 3-pulse laser spectroscopy to investigate how the ET from the dimethyl aniline (D) electron donor to the N-isopropyl-1,8-napthalimide (NAP) electron acceptor can be altered by exciting the C≡C stretching mode ($\nu_{C\equiv C}$) of the butadiyne bridge linking donor and acceptor. The electron transfer was initiated by electronically exciting the acceptor moiety at 400 nm, followed by vibrational excitation of the alkyne, $\nu_{C\equiv C}$, and detecting the changes in the absorption spectrum in the visible spectral region. The experiments were performed at different delay times t_1 and t_2, which are the delays between UV – mid-IR and mid-IR – Vis pulses, respectively. Two sets of torsion-angle conformers were identified, one featuring a very fast mean ET time of 0.63 ps (group A) and another featuring a slower mean ET time of 4.3 ps (group B), in the absence of the mid-IR excitation. TD-DFT calculations were performed to determine key torsion angle dependent molecular parameters, including the electronic and vibrational transition dipoles, transition frequencies, and the electronic couplings. To describe the 3-pulse data, we developed a kinetic model that includes a locally excited, acceptor-based S2 state, a charge separated S1 state, and their vibrationally excited counterparts, with either excited $\nu_{C\equiv C}$ (denoted as $S1A^{tr}$, $S1B^{tr}$, $S2A^{tr}$, $S2B^{tr}$, where tr stands for excited triplet bond, $\nu_{C\equiv C}$) or excited daughter modes of the $\nu_{C\equiv C}$ relaxation ($S1A^{h}$, $S1B^{h}$, $S2A^{h}$, $S2B^{h}$, where h stands for vibrationally hot species). The kinetic model was solved analytically, and the species-associated spectra (SAS) were determined numerically using a matrix approach, treating first the experiments with longer t_1 delays and then using the already determined SAS for modeling the experiments with shorter t_1 delays. Strong vibronic coupling of $\nu_{C\equiv C}$ and of vibrationally hot states make the analysis complicated. Nevertheless, the SAS of the were identified and the ET rates of the vibrationally excited species, $S2A^{tr}$, $S2B^{tr}$ and $S2B^{h}$, were determined. The results show that the ET rate for the S2A species is ca. 1.2-fold slower when the $\nu_{C\equiv C}$ mode is excited. The ET rate for species S2B is slower by ca. 1.3-fold if the compound is vibrationally hot and is essentially unchanged when the $\nu_{C\equiv C}$ mode is excited. The SAS determined for the tr and h species resemble the SAS for their respective precursor species in the 2-pulse transient absorption experiments, which validates the procedure used and the results.

* To whom correspondence should be addressed. E-mail: irubtsov@tulane.edu

1. Introduction

Electron transfer (ET) is a crucial process in chemistry and biology, and it is has important applications in catalysis, molecular electronics, and solar energy conversion.[1-3] An ability to manipulate ET rates using mid-IR excitation of vibrations can lead to the delicate control of kinetic processes.[4] Significant vibronic coupling is required to affect electronic wavefunctions through the excited vibrations. Numerous studies showed examples of systems featuring strong vibronic coupling,[5-13] and electron transfer between charge localized states involves non-adiabatic dynamics and failure of the Born-Oppenheimer approximation.[14] The presence of a range of molecular systems featuring strong vibronic interactions[15-20] and the dependence of ET rates on the vibrational quantum number of the reactant state [3] are encouraging for the study the ET rate modulation with vibrational excitation. Theoretical analysis revealed that ET dynamics can be modulated by controlling the coherence of inelastic tunneling pathways by excitation of a bridge vibration.[21-27]

We have reported on theoretical studies of how vibrational motion could modulate ET in donor–bridge–acceptor (DBA) compounds. Our studies have explored the possibility of manipulating the coupling pathway interferences for ET reactions through vibrational perturbations of the bridge.[21, 25] Two important conditions to produce potentially large effects through bridge vibrational perturbation were identified: the electron density on the bridge must be significant, and the electron transfer time should be shorter than vibrational relaxation.[28] We reported the first experimental measurement of ET rate modulation in a DBA complex with a Watson–Crick style hydrogen bonded guanosine - cytidine bridge by vibrational excitation of hydrogen bonded bridge modes where a reduction in the ET rate by ca. 60% was found.[29] ET modulation in other molecular systems were recently reported by Weinstein *et al.*,[30-32] Bakulin *et al.*,[33-35] and Rubtsov *et al*.[36]

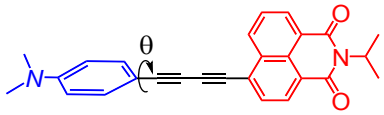

Figure 1. Structure of D-C4-NAP.

Here we describe ET rate modulation in D-C4-NAP (Fig. 1) in response to excitation of the C≡C symmetric stretching mode ($\nu_{C\equiv C}$) of the bridge. Alkyne moieties are attractive bridges for ET in DBA compounds, as they feature nearly linear structure and support strong coupling of electronic states across the bridge, thus supporting conditions for fast ET.[37-43] They also offer convenient vibrational modes to perturb the ET dynamics.[43] However, these bridges introduce complexity because of the strong torsion angle dependence of the ET rates and transition dipoles among electronic states and a shallow torsion barrier for rotation.[43]

We recently explored the ET dynamics in D-C4-NAP and related DBA complexes using 2-pulse UV-pump / Vis-probe and UV-pump / mid-IR-probe spectroscopies.[43] We found that the excited-state properties of D-C4-NAP, including the ET rate, depend strongly on the torsion angle, θ (Fig. 1). In the new studies reported here, we performed 3-pulse UV-pump / mid-IR-pump / Vis-probe transient absorption (TA) measurements (Section 2), quantum chemical analysis, and kinetic modeling (Section 3.3) to understand how vibrational excitation influences the excited state properties and the ET rate in D-C4-NAP. The modeling involved a matrix approach and determination of the species associated spectra (SAS) for all relevant species.

2. Experimental Details

The in-house-built experimental setup is described in ref. [43]. The laser pulses of 44 fs duration at 804 nm and 1 kHz repetition rate were produced by a Ti:Sapphire oscillator (Vitesse, Coherent Inc.) and a regenerative amplifier (Spitfire, Spectra Physics) tandem. A fraction of the beam (~150 μJ/pulse) was frequency doubled, resulting in UV pulses at 402 nm with 1–1.5 μJ energy per pulse, and was used to

excite the compounds electronically. Another fraction of the 800 nm beam (~500 μJ/pulse) was used to generate mid-IR pulses with an optical parametric amplifier and difference-frequency generation units. Mid-IR pulses tunable from 1000 to 4000 cm^{-1} were produced, featuring a spectral width of *ca.* 200 cm^{-1} and pulse energies of *ca.* 1.5 μJ at 2100 cm^{-1}. A small portion of the 804 nm beam (~10 μJ/pulse) was used to generate a white light continuum (WLC) in a sapphire wafer; the WLC served as a probe beam. A CCD camera (PIXIS-100, Princeton Instrument) mounted to a monochromator (TRIAX-190, Horiba) was used to measure the transient spectra in the visible region, while a single channel MCT detector (Infrared Associates) was used to measure spectra in the mid-IR region.

The time-delay diagram for the 3-pulse experiments is shown in Figure 2. The delay between the UV-pump that excites the compound electronically, and the mid-IR pump that perturbs it vibrationally is denoted t_1. The molecular system is then probed in the visible region by a pulse delayed by time t_2, referred to as the detection time.

The mid-IR beam was chopped with a mechanical chopper at half the repetition rate, and the absorbance difference (3-pulse transient absorption) was computed as a function of the wavelength as $\Delta A = A^{IR} - A$, where A^{IR} and A are the absorbances (optical densities) of the sample when the mid-IR pulse is present and absent, respectively. $\Delta A(t_1, t_2, \lambda)$ reports on the changes in the visible absorption of the compound induced in the molecular system by the mid-IR beam. Measurements at several fixed t_1 delays were performed where the t_2 delay was scanned in a wide range from 0 to ca. 2.5 ns, referred to as t_2-scan experiments.

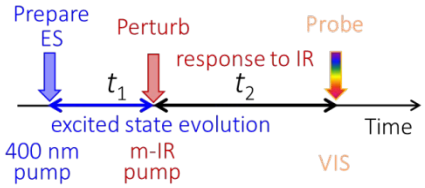

Figure 2. Time-delay diagram of the 3-pulse experiments.

For the spectroscopic measurements, the compound was dissolved in DCM at ca. 20 mM concentration. Full details on synthesis, structure and electrochemistry of the D-C4-NAP compound can be found in ref.[43, 44] Linear absorption measurements were performed in a sample cell with 1-mm-thick CaF_2 windows and an optical pathlength of 50 μm. The 3-pulse measurements were performed in a flow cell with 2-mm-thick CaF_2 windows and a 200 μm optical pathlength. The measurements were performed at room temperature, 22 ± 0.5 °C.

3. Results

3.1. Overview of 2-pulse TA dynamics of D-C4-NAP in DCM

Recent transient absorption experiments in the visible and mid-IR regions with a series of compounds featuring different donors, Si-C4-NAP, Ph-C4-NAP, and D-C4-NAP (where Si stands for trimethyl silane and Ph for phenyl moieties, Fig. S12), showed that the donor redox potential defines the character of the lowest singlet excited state as being NAP localized (Si-C4-NAP), partially polarized (Ph-C4-NAP), or, essentially, charge separated (CS; D-C4-NAP) state.[43] In the D-C4-NAP compound, the high donor strength produces decoupling of the S1 and S2 states, so that the S1 state has essentially pure CS character. Moreover, the CS state energy for D-C4-NAP in DCM is lower than the NAP-based triplet state energy.[43] Therefore, the excited-state reactions for D-C4-NAP in DCM are dominated by the CS and charge recombination (CR) processes in the singlet manifold. DFT analysis finds that the computed oscillator strengths of the S1 (CS) and S2 (NAP-based) states vary strongly with the torsion angle (θ, Fig. 1), and this effect is dictated by the symmetry of the frontier orbitals. The dependence is complementary: only the S1

state can be excited in the coplanar conformation, θ = 0, while only the S2 state can be excited in the orthogonal conformation.[43] As a result of this complementarity, and the closer match of the S2 state energy with 400 nm excitation, S2 states are dominantly produced by 400 nm and excitation, and those excited states feature the orthogonal conformations predominantly. In addition, the S2-S1 state coupling, which determines the CS reaction rate, is found to depend strongly on the torsion angle, resulting in a range of ET rates.

The decay-associated spectral analysis of the transient absorption data in the visible region following excitation at 400 nm showed three main spectral components associated with the exponential times of ca. 0.63, 4.3, and 260 ps (Fig. 3c). The slowest component is associated with the ground state (GS) recovery via the charge recombination reaction. The middle component, ca. 4.3 ps, was assigned to a slow electron transfer in conformations with a small S2-S1 coupling (θ ~ 0-15 and 63-90°). This time component is associated with spectacular changes in the mid-IR transient spectrum showing the appearance of a red-shifted peak at ca. 2030 cm^{-1} (Fig. 3e). The fastest component of 0.63 ps is associated with the CS reaction in conformations with smaller torsion angles featuring larger DA couplings. Kinetic spectral modeling, based on the DFT computed θ-dependent ground-state energy, S2 and S1 oscillator strengths, and C≡C vibrational frequencies and intensities, produced a good match with the experimental mid-IR spectra (Fig. 3e), thus confirming the assignment.

While the two fastest components are both associated with the CS reaction, just in different conformations, their manifestations in the transient spectra are drastically different. In the mid-IR region, the fast component is associated with a rise in the blue portion of the C≡C band, the 2085 cm^{-1} peak, and no change for the red peak at 2030 cm^{-1}. The slow component is characterized by a decay of the blue C≡C peak and a strong rise of the red peak. The spectral changes in the fingerprint region fully support the assignment that the two fast decay components, with time constants of 0.63 and 4.3 ps, as originating predominantly from the CS reaction for different θ conformers with θ ~ 15-63° and θ ~ 0-15 and 63-90°, respectively (Fig. 3e).[43] Because only a limited number of states can be identified experimentally, we divided all conformers into two groups. Group A involves conformers with θ ~ 15-63°, assigned a fast mean ET rate of 0.63 ps, and group B involves weakly coupled conformers (θ ~ 0-15 and 63-90°) featuring a slow mean ET rate of ca. 4.3 ps. A simplified kinetic scheme for the dominant processes is shown in Scheme 1.

$$\mathrm{S2A} \xrightarrow{k_{\mathrm{A}}} \mathrm{S1A} \xrightarrow{k_{\mathrm{CR,A}}}$$

$$\mathrm{S2B} \xrightarrow{k_{\mathrm{B}}} \mathrm{S1B} \xrightarrow{k_{\mathrm{CR,B}}}$$

Scheme 1. Kinetic scheme to describe 2-pulse TA signals. The k_{A}, k_{B} and $k_{\mathrm{CR,A}}$, $k_{\mathrm{CR,B}}$, rates denote the CS and CR rates, respectively, in the A and B groups of conformers.

Note that while the parallel kinetic scheme implemented here (Scheme 1) is much more difficult to treat compared to an all-sequential scheme, the latter cannot represent the torsion angle distribution. At the same time, introducing more groups of conformers than two, A and B, would result in an excessive number of modeling parameters to treat the presented spectroscopic data.

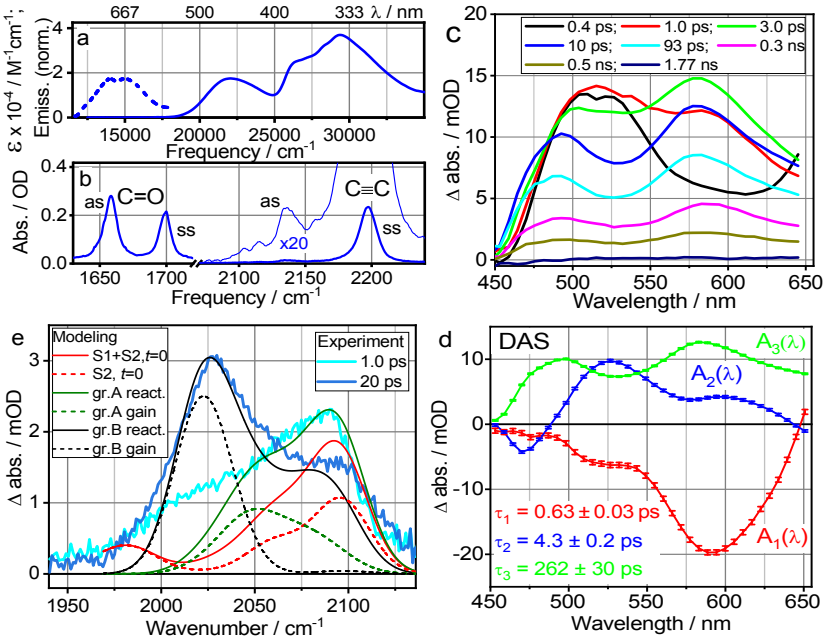

Figure 3. Linear absorption (solid line) and emission (dashed line) (a) and FTIR (b) spectra of D-C4-NAP in DCM; (c) 2-pulse TA spectra at delays specified as inset; (d) DAS for the measurments in panel (c) with time constants shown as inset. (e) 2-pulse TA mid-IR spectra at 1 and 20 ps. Spectral modeling is shown at t = 0 for S1 and S2 states together (red line) and for S2 contribution alone (red dashed line). Green line shows moddeled spectrum after ET group A completed; green dashed line shows the gain of S1 absorbance due to ET in group A. Black solid line shows the spectrum after ET is completed in group B; the gain of S1 absorbance due to ET in group B is shown by black dashed line.

3.2. 3-pulse t_2 scan measurements for D-C4-NAP.

The 3-pulse (UV / mid-IR / Vis) t_2 scan experiments were performed at different t_1 delays, so that the excited state dynamics is perturbed at different stages of the ET process. For example, if t_1 is smaller than the characteristic ET times in both conformer groups, both rates can potentially be altered by the mid-IR pulse. If, however, t_1 is significantly larger than the ET time in group A, the ET process for this group of conformers is completed by the time of mid-IR perturbation, so the mid-IR pulse will have no effect on the ET process in group A in those experiments. The mid-IR pulse spectrum in all experiments was centered in the C≡C stretching frequency region of the bridge (~2060 cm^{-1}).

The 3-pulse transient spectra acquired at different t_2 delays with the t_1 delay fixed at 2.5 ps are shown in Figure 4a. Transient kinetics at selected wavelengths (Fig. 4b) indicate the presence of multiple time components in the spectral evolution. A global fit of the transient spectra $S(t_2, \lambda)$ with a three-exponential function produced three decay-associated spectra (Fig. 4c) and three characteristic times: fast (τ_1 = 0.75 ± 0.02 ps), medium (τ_2 = 4.1 ± 0.5 ps), and slow (τ_3 = 12 ± 1 ps). Similar analysis was applied to the t_2-scan data measured at t_1 of 0.50, 10, 50, and 200 ps. The corresponding decay-associated spectra (DAS) and characteristic times are shown in Figure 5. To fit the 3-pulse spectra measured at longer t_1 delays ($t_1 \geq$ 10 ps), the three-exponential function was excessive, and a two-exponential function was used. Also, no more than three time components could be extracted with sufficient certainty from the data with t_1 values of 0.50 and 2.5 ps.

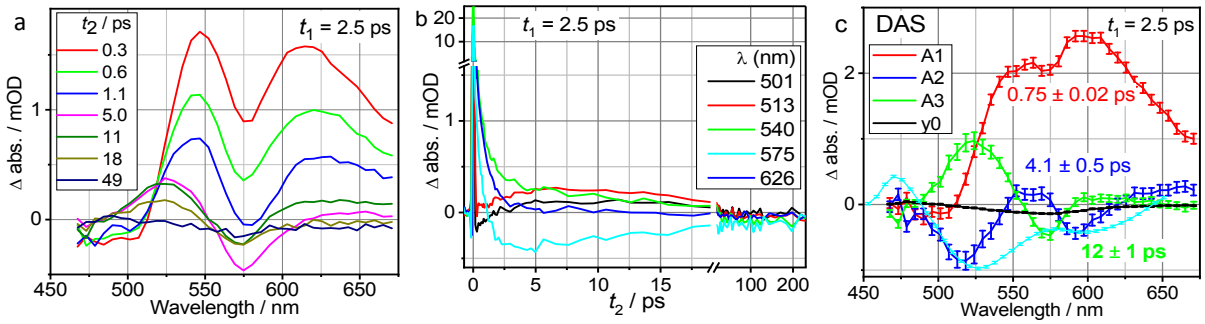

Figure 4. Selected 3-pulse t_2-scan transient spectra (a) and kinetics (b) measured at t_1 = 2.5 ps for D-C4-NAP in DCM. DAS with indicated characteristic times (c). The 2-pulse DAS of the 4.3 ps component (Fig. 3d), scaled by a factor of –0.1, is shown in panel (c) in cyan.

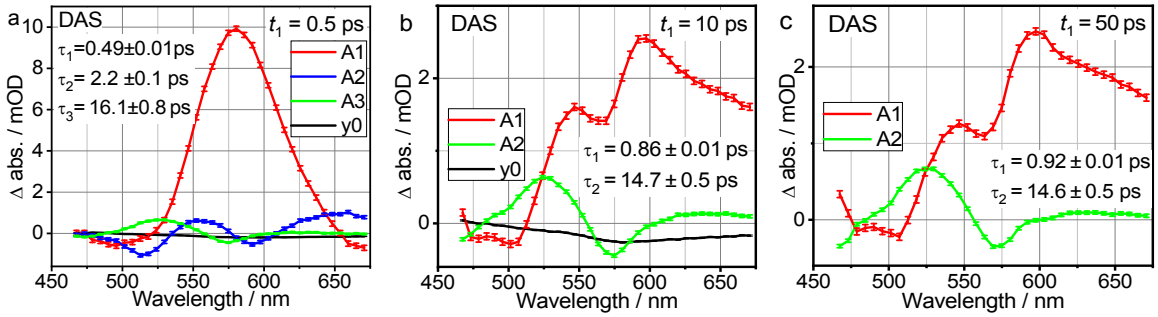

Figure 5. DAS obtained for the 3-pulse t_2-scan experiments at t_1 of (a) 0.5 ps, (b) 10 ps, and (c) 50 ps. The characteristic times are shown as insets.

We begin the discussion of the 3-pulse experiment results with the data measured at longer t_1 delays ($t_1 \geq 10$ ps), as the ET process is mostly completed for both the fast (A) and slow (B) reacting groups of conformers, and the system is in the S1 state at the time of the mid-IR pulse arrival. Indeed, the transient spectra measured at t_1 of 10, 50, and 200 ps are very similar, featuring a fast component of ca. 0.9 ps and a slow component of ca. 14.5 ps (Fig. 5b,c, Fig. S9).

The mid-IR pulse forms vibronic S1A^{tr} and S1B^{tr} states, where the tr superscript denotes excited C≡C triple-bond vibrations. The fast component of ca. 0.9 ps is assigned to the lifetime of the excited C≡C stretching mode in the S1 state of all electronically excited conformers. Relaxation of the S1A^{tr} and S1B^{tr} states produces hot (h) excited states S1A^{h} and S1B^{h}, where the excess energy is distributed in numerous vibrational degrees of freedom of the molecule. The slow component is assigned to vibrational cooling of the compound into the solvent, resulting in the decay of the S1A^{h} and S1B^{h} states. Note that the τ_2 decay time of 14.5 ps matches typical cooling times of organic compounds in the ground electronic state in non-H-bonding solvents, measured at ca. 14-15 ps.[45-47]

The kinetic scheme used to describe the 3-pulse spectra $t_1 \geq 10$ ps is shown in Scheme 2. Notice that the absence of (significant) transient signals with characteristic times slower than 14 ps suggests that the CR process is not affected measurably by the mid-IR excitation, indicating that $k_{CR,A} \approx k_{CR,A}^{tr} \approx k_{CR,A}^{h}$ and $k_{CR,B} \approx k_{CR,B}^{tr} \approx k_{CR,B}^{h}$. Therefore, the CR reaction rate altering with mid-IR is neglected for all 3-pulse experiments in this study. Notice that more elaborate kinetic schemes can be easily the

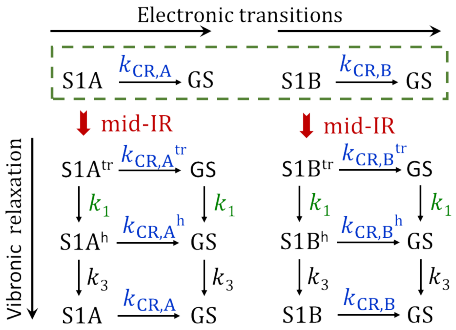

Scheme 2. Kinetic scheme to describe 3-pulse signals associated with evolution of the S1 excited state (experiments with $t_1 \geq 10$ ps). Electronic transitions evolve along the horizontal axis while vibronic transitions evolve in the vertical direction. The green box includes the reactions that occur without mid-IR excitation, serving as references.

The slowest DAS components in the t_1 = 0.5 ps and 2.5 ps data (green lines in Figs. 4c and 5a) are very similar in shape to the slowest DAS component in the data with $t_1 \geq 10$ ps (Fig. 5b,c), and the characteristic times are similar as well. Therefore, these components are also assigned to vibrational cooling of the compound by the solvent. The two faster DAS components in the t_1 = 0.5 and 2.5 ps spectra (red and blue lines in Figs. 4c and 5a) differ from each other and also are different from those in the $t_1 \geq 10$ ps data.

In the 3-pulse measurements at t_1 = 2.5 ps, the ET in the group A conformers is completed, while the ET is still ongoing in the group B conformers. The spectral shape and the decay time of the middle DAS component for t_1 = 2.5 ps (blue line in Fig. 4c) is similar to the shape and decay time of the (inverted) middle DAS component in the 2-pulse data; the latter was previously associated with ET in the group B conformers. This similarity suggests that the rate of ET in group B is altered by mid-IR excitation.

The fastest DAS component in the t_1 = 2.5 ps data (red line in Fig. 4c) resembles the fastest component in the t_1 = 10 and 50 ps data (red lines in Fig. 5b,c) in terms of peak positions, although the ratio of two constituent peaks and the overall shape are altered. In addition, the difference in their characteristic times, 0.75 ps vs. 0.9 ps, could be due to involvement of the ET process in group B. The modeling described below shows that it indeed originates from alteration of the k_B rate caused by the mid-IR excitation.

In the 3-pulse measurements at t_1 = 0.5 ps, the ET is not completed in either group of conformers at the time of the mid-IR pulse arrival, so both rates could be changed by the mid-IR pulse. The middle DAS component (blue line in Fig. 5a) resembles the middle DAS component of the t_1 = 2.5 ps data (blue line in Fig. 4c) and, as expected, has a larger absolute amplitude. As for the t_1 = 2.5 ps data, this component is assigned to the ET rate alteration in the group B conformers. The shape of the fastest DAS component in the t_1 = 0.5 ps data is different from the shapes of the DAS for component for t_1 = 50 ps and t_1 = 2.5 ps scans, and its amplitude is much higher than that of all other components. It peaks at ca. 580 nm, similar to that of the fast DAS in the 2-pulse experiment (Fig. 3b, red line), suggesting that it involves ET rate modulation in the group A conformers.

We used kinetic modelling to evaluate the modulated ET rates quantitatively. To assign spectral components to different species, we constructed species associated spectra (SAS) using the DAS and the kinetic model shown in Schemes 1 - 3. The 3-pulse data measured at larger t_1 delays were modeled first; the SAS obtained at longer t_1 data were used in the modeling of the 3-pulse spectra for smaller t_1 delays.

3.3. Kinetic modelling of the 2- and 3- pulse transient spectra.

Relationship between DAS and SAS. The relation between the DAS and SAS is seen from Eqs. 1-2, which express the transient absorption signals in terms of DAS (Eq. 1) and SAS (Eq. 2), respectively.[48-50] While the DAS represent just a fit of the data with a multi-exponential function (Eq. 1), each species associated spectrum, SAS_j, is multiplied by the respective concentration of the species, $n_j(t)$, (Eq. 2). As a result, the SAS are dependent on the kinetic scheme used to describe the process. The solution of a kinetic scheme, n_j, can be formulated in terms of a set of exponential terms (Eq. 3) with characteristic rates k_i.

$$TA(t) = \sum_{i=1}^{N_2} DAS_i(\lambda)\ exp\left(-k_i^{DAS}t\right) \quad (1)$$

$$TA(t) = \sum_{j=1}^{N} n_j(t)\ SAS_j(\lambda) \quad (2)$$

$$TA(t) = \sum_{j=1}^{N}\left(\sum_{i=1}^{N_1} P_{ji}\exp\left(-k_i t\right)\right) SAS_j(\lambda) \quad (3)$$

Here, N_2 is the number of the decay associated spectra, N is the number of species involved in the kinetic scheme, and N_1 is the number of different exponential terms obtained after solving the kinetic scheme. Equating the right sides of Eq. 1 and 3 we find:

$$\sum_{j=1}^{N}(\sum_{i=1}^{N_1} P_{ji}\ exp\ (-k_i t))\ SAS_j(\lambda) = \sum_{i=1}^{N_2} DAS_i(\lambda)\ exp\left(-k_i^{DAS}t\right) \quad (4)$$

For Eq. 4 to have a solution, the left and right sides must share the same set of rate constants. If N_2=N_1, the rate constants on the left side can be matched directly with those at the right side. If $N_2 \neq N_1$, the terms for more than one rate constant on the left or right side should be placed in correspondence with a single rate component on the other side. This process involves an approximation, and careful analysis of the rate constant values and the nature of the solution for the kinetic scheme. More details on establishing this relationship are given in the Supportive Information (Eq. S4 and S5). Equation 4 can be written in a matrix form as

$$SAS \times P = DAS \quad (5)$$

where SAS is a N_λ by N matrix of species associated spectra, DAS is a N_λ by N_2 matrix of decay associated spectra, P is the N by N_1 matrix of pre-exponentials defined from the selected kinetic scheme (Eq. 2-3), and N_λ is the number of wavelength points in the transient spectra. The $SAS(\lambda)$ can be determined from Eq. 6.

$$SAS(\lambda) = DAS(\lambda) \times P^{-1} \quad (6)$$

where the inverse P matrix is computed in MATLAB using a standard inverse function or a Moore-Penrose pseudoinverse function (pinv) to treat non-square P matrices.

Kinetic and spectral modelling of 2-pulse TA data. The kinetic scheme selected to describe the UV/Vis transient absorption measurements involves four species describing S1 and S2 states for each group of conformers (A and B; Scheme 1). By setting the charge recombination rate to be the same for both groups, the solution involves three rate constants, the same number as the number of DAS components (Scheme 1). The relative initial concentrations of the species, n_{S1A}, n_{S1B}, n_{S2A} and n_{S2B}, generated with 400 nm excitation, were determined using the linear absorption spectrum of the compound (Table 1 and Section S2). Using MATLAB, Equation 6 was solved, assuming that the spectra of S2A and S2B species are the same but allowing the S1A and S1B spectra to be different. The resulting SAS spectra of S1A and S1B appear to have the same shape, but sign inverted (similar in the mathematical sense but very different in the spectroscopic sense). Such result is an indication of the similarity of the two spectra, S1A and S1B. To reinforce the similarity and to avoid their complementarity, we have set the spectra of the S1A and S1B species to be the same. The resulting SAS are shown in Figure 6.

Natural transition orbitals (NTO) were computed for various electronic transitions using the TD-DFT method (see Section S10). The similarity of the NTO for S0→S1, S1→S2, and S1→S3 transitions supports the assignment of the same SAS for S1A and S1B species (Fig. S10-11). Note that the $SAS_{S1A/S1B}$ peak at

490 nm coincides with the previously reported peaks for isolated ion radicals $DMA^{+\bullet}$ [51-54] and 1,8-naphthalimide (NAPH-•)[55], analogous to NAP-•.

Table 1. Computed fractions of the involved species at different t_1 delays at the time of mid-IR excitation (t_2 = 0) and their fractions excited vibrationally.

Species	t_1 = 0	t_1 = 0.5 ps	t_1 = 2.5 ps	t_1 = 50 ps
n_{S2A}	0.400	0.181	0.0076	0
n_{S2B}	0.475	0.423	0.266	0
n_{S1A}	0.105	0.323	0.493	0.418
n_{S1B}	0.021	0.073	0.229	0.416
$n^{\mathrm{tr}}_{\mathrm{S2A}}$	-	0.0054	0	0
$n^{\mathrm{tr}}_{\mathrm{S2B}}$	-	0.013	0.0067	0
$n^{\mathrm{tr}}_{\mathrm{S1A}}$	-	0.021	0.025	0.021
$n^{\mathrm{tr}}_{\mathrm{S1B}}$	-	0.0047	0.014	0.023

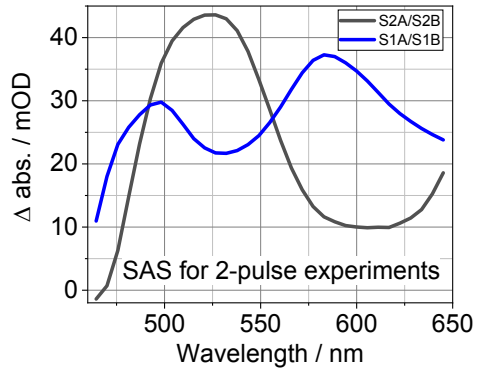

Figure 6. SAS for the S2A / S2B, and S1A / S1B species obtained from the modeling of the 2-pulse TA data.

Calculating relative fractions of different species at t_2 = 0 and different t_1 delays. The relative concentrations of the $S2A^{tr}$, $S2B^{tr}$, $S1A^{tr}$, and $S1B^{tr}$ species prepared by the mid-IR pulse arriving at delay time t_1 were calculate using the DFT-computed IR intensities of $\nu_{C\equiv C}$ as a function of θ ($f^{\mathrm{tr}}_{\mathrm{S1}}(\theta)$ and $f^{\mathrm{tr}}_{\mathrm{S2}}(\theta)$). Eq. 7 shows how to compute $n^{\mathrm{tr}}_{\mathrm{S2A}}$ at t_2 = 0; equations for other species are similar.

$$n^{\mathrm{tr}}_{\mathrm{S2A}}(t_1, t_2 = 0) = \sum_{\theta \in \mathrm{Gr.\,A}} n_{\mathrm{S2A}}(t_1 = 0,\theta) \cdot F_{\mathrm{S2A}}(t_1) \cdot f^{\mathrm{tr}}_{\mathrm{S2}}(\theta) \qquad (7)$$

Here the $F_{\mathrm{S2A}}(t_1)$ function describes the kinetics of the S2A species (the fraction of S2A species at the t_1 delay after UV pump), obtained from solving the kinetic scheme for the 2-pulse measurements (Scheme 1, Eq. S7-S8). The product, $n_{\mathrm{S2A}}(0,\theta) \cdot F_{\mathrm{S2A}}(t_1)$, represents the concentration of the S2A species at t_1. By multiplying this product by scaled IR intensity of the $\nu_{C\equiv C}$ transition, $f^{\mathrm{tr}}_{\mathrm{S2}}(\theta)$, the relative fraction of S2A states at torsion angle θ with $\nu_{C\equiv C}$ excited is obtained. Summation over θ for the angles belonging to the specified group (group A in Eq. 7) results in a final relative fraction of $\nu_{C\equiv C}$-excited molecules in the specified state and group, $n^{\mathrm{tr}}_{\mathrm{S2A}}(t_1, t_2 = 0)$, which is the initial concentration of the species for the dynamics during the t_2 time interval. The same calculations were performed for all species and for all experimental t_1 values (Table 1).

Modeling 3-pulse data with $t_1 \geq 10$ ps. The kinetic scheme used to describe the processes at $t_1 \geq 10$ ps is shown in Scheme 2, and is shown in a simplified manner in Scheme 3a,b. The participation of the S1A and S1B species with and without mid-IR excitation was considered. With mid-IR excitation, certain fractions of S1A and S1B are converted to their tr species, $S1A^{tr}$ and $S1B^{tr}$. The $S1A^{tr}$ and $S1B^{tr}$ species relax into $S1A^{h}$ and $S1B^{h}$ species (k_1), which relax further into S1A and S1B, respectively (k_3). As the number of rate constants (k_1 and k_3) equals the number of DAS components, their correspondence is straight forward, $k_1 = k_1^{DAS}$ and $k_3 = k_2^{DAS}$, so is the use of Eq. 6 to obtain SAS of the $S1A^{tr}$, $S1A^{h}$, $S1B^{tr}$, and $S1B^{h}$ species (Fig. 7a).

The obtained SAS of the $S1A^{tr}$ and $S1B^{tr}$ states have nearly the same shapes and amplitudes (Fig. 7a; blue and black lines); their shapes are also similar to the shape of the fast component of the DAS (Fig. 5b,c). The SAS shapes for the $S1A^{h}$ and $S1B^{h}$ species are similar to each other (Fig. 7a, red and green lines) and also similar to the DAS of the slow component in the 2-pulse experiments (Fig. 5b,c).

The SAS spectra of $S1A^{tr}$, $S1B^{tr}$, $S1A^{h}$, and $S1B^{h}$ species (Fig. 7a) show similar peaks with the S1A and S1B spectra (Fig. 6), but the former are slightly red shifted, likely due to the vibronic interactions in the vibrationally excited S1 state.

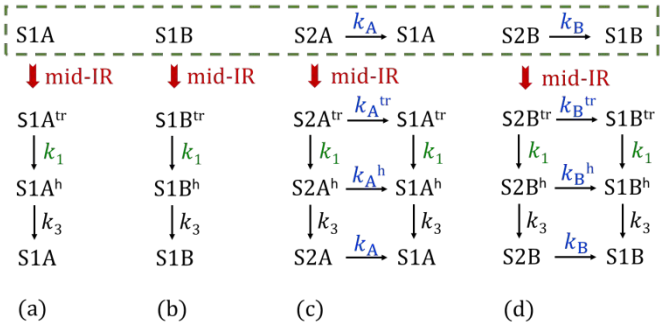

Scheme 3. Kinetic scheme used to describe the CS reaction in the 3-pulse experiments. The green box indicates the reactions without mid-IR excitation, which served as references.

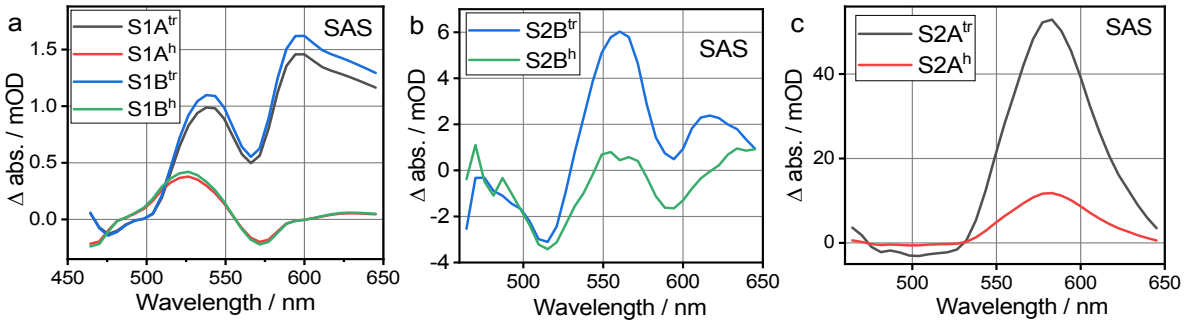

Fig. 7. SAS of the indicated species determined from (a) t_1 = 50 ps, (b) t_1 = 2.5 ps, and (c) t_1 = 0.5 ps 3-pulse experiments.

Modeling 3-pulse data with t_1 = 2.5 ps. The three species present in the system at t_1 = 2.5 ps for mid-IR excitation are S1A, S1B, and S2B, so reactions in panels a, b, and d of Scheme 3 contribute to the 3-pulse TA signals. The initial concentrations of these species (Table 1) were computed using the kinetic equations of Scheme 1. The excitation probabilities to form $S1A^{tr}$, $S1B^{tr}$, and $S2B^{tr}$ were computed in the same way as described earlier. The difference from the data with t_1 = 50 ps is in the presence of the $S2B^{tr}$ and $S2B^{h}$ species, which can undergo ET with a different rate than k_B, denoted k_B^{tr} and k_B^{h}. The presence of $S2B^{tr}$ and $S2B^{h}$ can also simply change the visible absorption spectrum of the compound due to vibronic

coupling, but the characteristic times expected are ca. 0.9 ps and 14.5 ps (Fig. 5b,c). Also, the characteristic spectra of the vibronic coupling contributions are rather characteristic (Fig. 5b,c), while the second DAS of the t_1 = 2.5 data (Fig. 4c) shows significant deviation from such spectral shape.

The analytical solution for the proposed scheme produces four different exponential terms: exp(-k_1*t), exp(-k_3*t), exp(-(k_1 + k_B^{tr})*t) and exp(-(k_3 + k_B^{h})*t). Because the number of rate components in the DAS (three) does not match the number of exponential terms in the kinetic scheme, an approximation needs to be introduced. Note that the fit of the experimental data with a four-exponential function cannot be used due to a strong dependence of the obtained parameters and large error bars on the rates and DAS. The approximation we implemented involves a conversion of the results predicted by the kinetic scheme to contain only three exponential terms, which can then be matched with the DAS rates. Analysis of the four exponential terms involved revealed that two of them, k_1 + k_B^{tr} and k_1, are expected to have similar values because k_1 >> k_B^{tr}, as k_1 = (0.9 ps)$^{-1}$, obtained from t_1 = 50 ps data, and k_B^{tr} is about (4 ps)$^{-1}$. Therefore, we assigned both k_1 + k_B^{tr} and k_1 as k_1^{DAS} (see SI for details). The slowest process, k_3, is assigned to k_3^{DAS}, which is the same as the slowest component in the t_1 = 50 ps experiments. The remaining component, k_3 + k_B^{h}, is associated as k_2^{DAS}. The validity of the approximation was tested by comparing the raw data with the computed t_2-dependent 3-pulse transient spectra using the kinetic scheme solution (Eq. S10-S18) but with altered rate constant (k_1 = (0.75 ps)$^{-1}$). The comparison revealed that a good match was obtained (Fig. S5). The solution of the resulting equation is now straight forward using Eq. 6, as the number of exponential terms on the left and right sides of Eq. 6 are the same and the model includes a small number of species with unknown spectra, S2B^{tr} and S2B^{h}. The resulting SAS of S2B^{tr} and S2B^{h} are shown in Fig. 7b. The assignment of k_1 + k_B^{tr} as k_1^{DAS} and k_3 + k_B^{h} as k_2^{DAS} results in the following k_B^{tr} and k_B^{h} values: k_B^{tr} = (4.0 ps)$^{-1}$, k_B^{h} = (5.7 ps)$^{-1}$. The value of k_B^{h} obtained is ca. 1.31 $\pm$ 0.27 times smaller than k_B = (4.3 ps)$^{-1}$ that indicates gentle modulation of the ET rate in vibrationally hot molecules of group B (see SI for error bar evaluation procedure). The k_B^{tr} value is similar to k_B, suggesting an insignificant modulation of the ET rate by exciting the C≡C mode. The obtained SAS for S2B^{tr} and S2B^{h} have similar shapes with peaks at ca. 560 nm and 610 nm (Fig. 7b). These peaks appear to be red shifted compared to the peak of SAS for S2B, at 525 nm, likely due to vibronic interactions in the vibrationally excited S2 state.

Modeling 3-pulse data with t_1 = 0.5 ps. All four species, S1A, S1B, S2A, and S2B, are present in the sample 0.5 ps after UV excitation, so all reactions outlined in Scheme 3 contribute. The analytical solution contains six different rate constants, k_1, k_3, $k_1 + k_B^{tr}$, $k_3 + k_B^{h}$, $k_1 + k_A^{tr}$, and $k_3 + k_A^{h}$ (Eqs. S13-S16), which is too many to treat directly using Eq. 6. The approach we took is to use the analytical solution and the already determined SAS and rates. We then introduced the information to Eq. 3 for TA(t). The simplification performed numerically led to Eq. S25, that equates the reduced TA spectrum, TA^{r}(t), to the terms involving only two unknown rate constants, $k_1 + k_A^{tr}$ and $k_3 + k_A^{h}$, multiplied by yet undetermined SAS of S2A^{tr} and S2A^{h} and already known SAS of S1A^{tr} and S1A^{h} species. The TA^{r}(t) data were fitted globally using a two-exponential function, leading to two rate constants that are the same within the error bars, (0.421 $\pm$ 0.004 ps)$^{-1}$ and (0.426 $\pm$ 0.006 ps)$^{-1}$. A matrix equation resulted, similar to Eq. 5, which was solved using Eq. 6. The SAS portion of the matrix equation contains a combination of unknown SAS and known SAS; the former were obtained by subtracting the latter from the result (Eq. S26). Note that all of the laser experiments were performed for the same sample with the same experimental conditions, so the procedure that was performed is viable. In addition, at the last subtraction step, the contributions of the S1A^{tr} and S1A^{h} species were over an order of magnitude smaller than those from the S2A^{tr} and S2A^{h} species. The SAS obtained for S2A^{tr} and S2A^{h} species appeared to be very similar in shape but opposite in sign. The closeness of the two characteristic times and the similarity in the SAS shapes suggest that the data can likely be fitted well with a single exponential function. Indeed, such fit resulted in a root-mean-square error of 0.0289, compared to 0.0288 for the two-exponential fit, and the characteristic time of 0.420 $\pm$ 0.002 ps. The resulting SAS were very similar to the ones obtained using the two-exponential fit, which allows us to

conclude that either the SAS of S2A^{tr} and S2A^{h} are very similar, or that the one of the two species is not contributing much to the observed signals. Indeed, the latter is likely to be true with the S2A^{h} species contributing little as the ET rate of S2A^{tr} is larger than the rate of formation of S2A^{h}. Therefore, the observed rate was assigned to $k_1 + k_{\mathrm{A}}^{\mathrm{tr}}$, resulting in $k_{\mathrm{A}}^{\mathrm{tr}}$ of (0.77 $\pm$ 0.05 ps)$^{-1}$ (Table 2), which is slower that k_{A} by a factor of 1.22 $\pm$ 0.14. We cannot determine the $k_{\mathrm{A}}^{\mathrm{h}}$ value with sufficient precision, as the reaction involving this rate constant does not contribute much to the overall process. The obtained SAS of S2A^{tr} is broad with a peak at 580 nm (Fig. 7c), resembling the 2-pulse SAS of S2A, that peaks at 525 nm, suggesting that the $\nu_{C\equiv C}$ excitation causes a shift and strengthening of the absorption of S2A species in the visible region.

Table 2. Characteristic ET rates for the two groups of conformers (*i* = A, B) with the $\nu_{C\equiv C}$ excited (k_i^{tr}), vibrationally hot (k_i^h), and relaxed (k_i).

Conformers	k_i, ps^{-1}	k_i^{tr}, ps^{-1}	k_i^h, ps^{-1}
Group A	1.59 ± 0.075	1.30 ± 0.096	--
Group B	0.230 ± 0.010	0.24 ± 0.034	0.175 ± 0.036

The SAS presented in Figures 6 and 7 can be called difference SAS as they are referenced to the respective state lacking vibrational excitation. For example, the SAS of S2A^{tr} and S2A^{h} species are referenced to the absorption spectrum of the S2A species.

4. Discussion

The 3-pulse UV / mid-IR / Vis experiments for D-C4-NAP revealed complex dynamics caused by strong vibronic couplings of the mode initially excited with mid-IR ($\nu_{C\equiv C}$) and its relaxation daughter modes. The vibronic coupling masks the signals associated with ET products making it difficult to isolate them and to characterize the ET reaction. Therefore, extended kinetic schemes were implemented that involve the species with excited $\nu_{C\equiv C}$ (tr excited) as well as species with excited daughter modes produced by $\nu_{C\equiv C}$ relaxation (vibrationally hot states). Moreover, the ET was found to be torsion-angle dependent, which was modelled by introducing two groups of conformers, a fast reacting group A and a slow reacting groups B. The kinetic scheme was solved stepwise beginning with the experiments at longer t_1 delays as a smaller number of species was involved in those measurements. The SAS of the involved species were determined from these experiments using a matrix approach and an in-house written MATLAB code. To model the experiments at smaller t_1 delays, the SAS of the already determined species were used.

Experimental results for t_1=50 ps scans were used to determine the vibrational relaxation rates and SAS of vibronic species (tr and h) in the S_1 state. The two main peaks of the SAS for these vibronic species in the S1 state are red shifted compared to SAS for just the S1 state, likely due to vibronic interactions in the vibrationally excited S1 state. The obtained SAS were implemented iteratively using first for the t_1 = 50 ps experiments and then for the t_1 = 2.5 ps experiments to determine the SAS of vibronic species (tr and h) of B and A in the S2 state, respectively, as well as the corresponding rate constants. The shapes of the SAS of the vibronic species for the S2 state match the SAS of their relevant parent species well (either A or B in the S2 state) exhibiting red shifted peaks due to vibronic interactions.

The modeling shows no significant changes in the ET rate in group B (slow ET) when the $\nu_{C\equiv C}$ mode was excited, which is likely affected by a mismatch in the $\nu_{C\equiv C}$ mode lifetime and the mean ET rate in group B. However, the ET rate in group B is affected by the vibrationally hot compounds (S2B^{h}), becoming 1.31 $\pm$ 0.27 times slower. These results suggest that there are vibrational modes in the compound that can alter the ET rate much stronger than $\nu_{C\equiv C}$ does. Because of the overall ET time is short, ~4 ps, these daughter modes are likely located within the butadiyne bridge. The fast ET in group A was found to be affected by excitation of the $\nu_{C\equiv C}$ mode, which makes the rate slower by a factor of 1.22 $\pm$ 0.14. Overall, the ET rate modulation is modest (see Table 2) despite rather strong transient spectra observed (Figs. 5, 4c);

yet the changes appearing in the spectra and kinetics due to ET are well characterized in the 3-pulse experiments. The ET rate slowing, found for both $\nu_{C\equiv C}$ mode and its relaxation daughter modes, emphasizes the potential of the butadiyne bridges for ET modulation. Note that no modulation of the CR rate was observed, likely due to a large mismatch between the vibrational lifetimes (~1 ps for $\nu_{C\equiv C}$ and ~14 ps for cooling of the $\nu_{C\equiv C}$ daughter modes) and the rate of CR, $(263\ ps)^{-1}$.

To conclude, we found that even if the 3-pulse spectra for a DBA compound show very prominent signals, they do not necessarily report on the ET rate modulation. This is especially so in DBA compounds with conjugated bridges which support stronger D-A coupling. However, as the D-A coupling increases, the vibronic coupling increases as well, masking the ET related signals. We presented a novel step-by-step matrix-based modeling approach to treat the 3-pulse data in the presence of severe vibronic coupling. The modeling revealed that while the vibronic coupling dominates the 3-pulse signals, the ET rate modulation is apparent, revealing the slowing of the ET rates by a factor of ca. 1.2-1.3. The presented approach helps understanding the vibronic coupling contributions to the transient 3-pulse spectra, which is essential for isolating the ET dynamics.

Conflicts of interest. The authors declare no conflicts of interest.

Acknowledgements

Support from the National Science Foundation (CHE-1954853 to IVR, CHE-1955138 to DNB, PZ and JV, and CHE-2102049 to TR) is gratefully acknowledged.

References

1. M. Natali, S. Campagna and F. Scandola, *Chem. Soc. Rev.*, 2014, **43**, 4005-4018.
2. S. Dadashi-Silab, S. Doran and Y. Yagci, *Chem. Rev.*, 2016, **116**, 10212-10275.
3. K. G. Spears, X. Wen and R. Zhang, *J. Phys. Chem.*, 1996, **100**, 10206-10209.
4. Z. Ma, Z. Lin, C. M. Lawrence, I. V. Rubtsov, P. Antoniou, S. S. Skourtis, P. Zhang and D. N. Beratan, *Chem. Sci.*, 2018, **9**, 6395-6405.
5. P. F. Barbara, T. J. Meyer and M. A. Ratner, *J. Phys. Chem.*, 1996, **100**, 13148-13168.
6. J. N. Schrauben, K. L. Dillman, W. F. Beck and J. K. McCusker, *Chem. Sci.*, 2010, **1**, 405-410.
7. G. Auböck and M. Chergui, *Nat. Chem.*, 2015, **7**, 629-633.
8. P. J. Johnson, A. Halpin, T. Morizumi, V. I. Prokhorenko, O. P. Ernst and R. D. Miller, *Nat. Chem.*, 2015, **7**, 980-986.
9. S. Kohler, J. Lehmann and P. Hänggi, *Phys. Rep.*, 2005, **406**, 379-443.
10. J. B. Maddox, U. Harbola, N. Liu, C. Silien, W. Ho, G. C. Bazan and S. Mukamel, *J. Phys. Chem. A*, 2006, **110**, 6329-6338.
11. A. Troisi, J. M. Beebe, L. B. Picraux, R. D. Van Zee, D. R. Stewart, M. A. Ratner and J. G. Kushmerick, *Proc. Natl. Acad. Sci. U.S.A.*, 2007, **104**, 14255-14259.
12. P. P. Roy, S. Kundu, J. Valdiviezo, G. Bullard, J. T. Fletcher, R. Liu, S.-J. Yang, P. Zhang, D. N. Beratan and M. J. Therien, *J. Am. Chem. Soc.*, 2022, **144**, 6298-6310.
13. B. C. Paulus, S. L. Adelman, L. L. Jamula and J. K. McCusker, *Nature*, 2020, **582**, 214-218.
14. A. Nitzan, *Chemical dynamics in condensed phases: relaxation, transfer and reactions in condensed molecular systems*, Oxford university press, 2006.
15. E. Romero, R. Augulis, V. I. Novoderezhkin, M. Ferretti, J. Thieme, D. Zigmantas and R. Van Grondelle, *Nat. Phys.*, 2014, **10**, 676-682.

16. F. D. Fuller, J. Pan, A. Gelzinis, V. Butkus, S. S. Senlik, D. E. Wilcox, C. F. Yocum, L. Valkunas, D. Abramavicius and J. P. Ogilvie, *Nat. Chem.*, 2014, **6**, 706-711.
17. T. A. Oliver and G. R. Fleming, *J. Phys. Chem. B*, 2015, **119**, 11428-11441.
18. V. Tiwari, W. K. Peters and D. M. Jonas, *Proc. Natl. Acad. Sci. U.S.A.*, 2013, **110**, 1203-1208.
19. N. Christensson, H. F. Kauffmann, T. Pullerits and T. Mancal, *J. Phys. Chem. B*, 2012, **116**, 7449-7454.
20. A. Chin, J. Prior, R. Rosenbach, F. Caycedo-Soler, S. F. Huelga and M. B. Plenio, *Nat. Phys.*, 2013, **9**, 113-118.
21. S. S. Skourtis, D. H. Waldeck and D. N. Beratan, *J. Phys. Chem. B*, 2004, **108**, 15511-15518.
22. M. D. Newton, *Int. J. Quantum Chem.*, 2000, **77**, 255-263.
23. H. B. Gray and J. R. Winkler, *Q. Rev. Biophys.*, 2003, **36**, 341-372.
24. E. S. Medvedev and A. A. Stuchebrukhov, *J. Chem. Phys.*, 1997, **107**, 3821-3831.
25. D. Xiao, S. S. Skourtis, I. V. Rubtsov and D. N. Beratan, *Nano Lett.*, 2009, **9**, 1818-1823.
26. D. N. Beratan, S. S. Skourtis, I. A. Balabin, A. Balaeff, S. Keinan, R. Venkatramani and D. Xiao, *Acc. Chem. Res.*, 2009, **42**, 1669-1678.
27. S. S. Skourtis and D. N. Beratan, *Adv. Chem. Phys.: Electron Transfer—from Isolated Molecules to Biomolecules. Part 1*, 1999, **106**, 377-452.
28. P. Antoniou, Z. Ma, P. Zhang, D. N. Beratan and S. S. Skourtis, *Phys. Chem. Chem. Phys.*, 2015, **17**, 30854-30866.
29. Z. Lin, C. M. Lawrence, D. Xiao, V. V. Kireev, S. S. Skourtis, J. L. Sessler, D. N. Beratan and I. V. Rubtsov, *J. Am. Chem. Soc.*, 2009, **131**, 18060-18062.
30. M. Delor, P. A. Scattergood, I. V. Sazanovich, A. W. Parker, G. M. Greetham, A. J. Meijer, M. Towrie and J. A. Weinstein, *Science*, 2014, **346**, 1492-1495.
31. M. Delor, T. Keane, P. A. Scattergood, I. V. Sazanovich, G. M. Greetham, M. Towrie, A. J. Meijer and J. A. Weinstein, *Nat. Chem.*, 2015, **7**, 689-695.
32. M. Delor, S. A. Archer, T. Keane, A. J. Meijer, I. V. Sazanovich, G. M. Greetham, M. Towrie and J. A. Weinstein, *Nat. Chem.*, 2017, **9**, 1099-1104.
33. A. A. Bakulin, R. Lovrincic, X. Yu, O. Selig, H. J. Bakker, Y. L. Rezus, P. K. Nayak, A. Fonari, V. Coropceanu and J.-L. Brédas, *Nat. Commun.*, 2015, **6**, 1-8.
34. A. A. Bakulin, R. Lovrinčić, Y. Xi, O. Selig, H. J. Bakker, Y. L. Rezus, P. K. Nayak, A. Fonari, V. Coropceanu and J.-L. Brédas, *arXiv preprint arXiv:1503.00777*, 2015.
35. A. A. Bakulin, R. Lovrincic, A. Rao, S. Gelinas, Y. Xi, O. Selig, Z. Chen, R. H. Friend, H. J. Bakker and D. Cahen, Ultrafast Phenomena XIX: Proceedings of the 19th International Conference, Okinawa Convention Center, Okinawa, Japan, July 7-11, 2014, 2015.
36. Y. Yue, T. Grusenmeyer, Z. Ma, P. Zhang, R. H. Schmehl, D. N. Beratan and I. V. Rubtsov, *Dalton Trans.*, 2015, **44**, 8609-8616.
37. M. Kivala and F. Diederich, 2009.
38. N. M. Dickson-Karn, C. M. Olson, W. C. Leu and C. S. Hartley, *J. Phys. Org. Chem.*, 2014, **27**, 661-669.
39. R. Wang, A. M. Brugh, J. Rawson, M. J. Therien and M. D. Forbes, *J. Am. Chem. Soc.*, 2017, **139**, 9759-9762.
40. M. Hoffmann, J. Kärnbratt, M. H. Chang, L. M. Herz, B. Albinsson and H. L. Anderson, *Angew. Chem. Int. Ed.*, 2008, **47**, 4993-4996.
41. S. Priyadarshy, M. J. Therien and D. N. Beratan, *J. Am. Chem. Soc.*, 1996, **118**, 1504-1510.
42. S. D. Banziger, X. Li, J. Valdiviezo, M. Zeller, P. Zhang, D. N. Beratan, I. V. Rubtsov and T. Ren, *Inorg. Chem.*, 2019, **58**, 15487-15497.
43. X. Li, J. Valdiviezo, S. D. Banziger, P. Zhang, T. Ren, D. N. Beratan and I. V. Rubtsov, *Phys. Chem. Chem. Phys.*, 2020, **22**, 9664-9676.

44. S. D. Banziger, R. A. Clendening, B. M. Oxley and T. Ren, *J. Phys. Chem. B*, 2020, **124**, 11901-11909.
45. N. I. Rubtsova and I. V. Rubtsov, *Annu. Rev. Phys. Chem.*, 2015, **66**, 717-738.
46. Z. Lin, P. Keiffer and I. V. Rubtsov, *J. Phys. Chem. B*, 2011, **115**, 5347-5353.
47. I. V. Rubtsov and A. L. Burin, *J. Chem. Phys.*, 2019, **150**, 020901.
48. C. Consani, G. Auböck, O. Bräm, F. Van Mourik and M. Chergui, *J. Chem. Phys.*, 2014, **140**, 01B605_601.
49. I. H. M. van Stokkum, D. S. Larsen and R. van Grondelle, *Biochim Biophys Acta Bioenerg*, 2004, **1657**, 82-104.
50. J. M. Beechem and E. Gratton, *Fluorescence spectroscopy data analysis environment: a second generation global analysis program*, SPIE, Los Angeles, California, United States, 1988.
51. K. Yoshihara, Y. Nagasawa, A. Yartsev, A. E. Johnson and K. Tominaga, in *Studies in Physical and Theoretical Chemistry*, Elsevier, 1995, vol. 83, pp. 59-64.
52. V. Saik, A. Goun and M. Fayer, *J. Chem. Phys.*, 2004, **120**, 9601-9611.
53. H. Kandori, K. Kemnitz and K. Yoshihara, *J. Phys. Chem.*, 1992, **96**, 8042-8048.
54. I. V. Rubtsov, H. Shirota and K. Yoshihara, *J. Phys. Chem. A*, 1999, **103**, 1801-1808.
55. B. M. Aveline, S. Matsugo and R. W. Redmond, *J. Am. Chem. Soc.*, 1997, **119**, 11785-11795.